On the Global Behavior of a Geometric PDAV Controller by Means of a Geometrically Exact Linearization

Michalis Ramp[1]
Department of Mechanical Engineering,
National Technical University of Athens,
9 Heroon Polytechniou Str.,
Athens 15780, Greece
e-mail: rampmich@central.ntua.gr

Evangelos Papadopoulos
Fellow ASME
Department of Mechanical Engineering,
National Technical University of Athens,
9 Heroon Polytechniou Str.,
Athens 15780, Greece
e-mail: egpapado@central.ntua.gr

A complex motion encountered in a number of robotic, industrial, and defense applications is the motion of a rigid body when one of its body-fixed axes tracks a desired pointing direction while it rotates at high angular velocity around the pointing direction (PDAV); during this motion, high frequency precession/nutation oscillations arise. This work analyzes the global/local closed-loop (CL) behavior induced by a developed geometric, PDAV controller and studies the high frequency precession/nutation oscillations that characterize PDAV motions. This is done via geometrically exact linearization and via simulation techniques that amount to charting the smooth CL vector fields on the manifold. A method to quickly estimate the frequency of the precession/nutation oscillations is developed and can be used for sizing actuators. A thorough understanding of the behavior of the CL flow induced by the PDAV controller is achieved, allowing the control engineer to anticipate/have a rough estimate of the system CL response.
[DOI: 10.1115/1.4049552]

Introduction

A common task encountered in a number of important applications is the motion performed by a rigid body when one of its body-fixed axes tracks a desired pointing direction and simultaneously, its angular velocity around the pointing direction (PDAV) is controlled to a desired reference. PDAV applications include surveillance apparatuses like radar or sonar sensors, satellite attitude control, modern rail guns, oil drilling rigs, three-dimensional (3D) computer numerical control machines, and tiltrotor aircrafts [1]. Vectored actuation by pointing a rotating high-speed propeller is employed frequently for thrust control in underwater/aerial robotics [2,3].

Despite the fact that the closely related problem of pointing direction stabilization (in which the angular velocity is regulated to zero) has received heavy attention [1,2,4–10], only few works study the PDAV control problem explicitly. Selected works include Refs. [3,11,12].

A critical issue in attitude control is that the topology of the configuration manifold of rigid body attitude dynamics prohibits the design of a continuous/smooth asymptotic global controller [13]. This holds regardless of the choice of attitude representation [14]. In attitude controls, this limitation is handled by two approaches. In the first approach, global control systems are obtained via switching algorithms [10,11,15–17]. These solutions need careful implementation due to switching complications. In the second approach, smooth attitude control systems are designed, guaranteeing almost global asymptotic stability [3,7–9,12,18–22]. However, the region of attraction excludes a set of zero measure comprised by the stable manifolds of the systems saddle equilibria (SMSE) [18]. The influence of this set on the closed-loop (CL) response and on the way the states are affected when they approach the SMSE set is not understood well. Recently, the influence of the SMSE set on the CL behavior for a mUAV outrunner/propeller assembly under PDAV control [23], and for the attitude control systems of a spherical pendulum and of a 3D pendulum was investigated [24]; the analysis in both [23,24] showed the nontrivial influence of these sets on the evolution of the CL flow.

This work aims to understand the global stabilization behavior of the PDAV CL dynamics induced by the controller in Ref. [3], to study the PDAV trajectory tracking motion characterized by high frequency precession/nutation oscillations, and since the controller has an almost global region of attraction, to investigate how the PDAV CL behavior of a general PDAV system is affected by the SMSE set induced by the controller in Ref. [3].

This is achieved via a geometrically exact linearization (a linearization on the tangent bundle using the exponential map), by showing that the system is state-constrained controllable, by obtaining estimates of the high frequency precession/nutation oscillations arising during PDAV tracking, and by means of variational integration techniques that amount to charting the smooth CL vector fields and allow the investigation of the impact of the SMSE set on the evolution of the global CL flow.

Knowledge of the behavior of the smooth CL vector fields emanating from a neighborhood of the SMSE set and from a neighborhood of the desired equilibrium allows the control engineer to have a rough estimate/"anticipate" the system CL response. The ability to quickly estimate the frequency of the precession/nutation oscillations allows proper actuator/drive sizing and trajectory/control design for PDAV applications. Finally, the obtained results are applicable to any system that employs the PDAV controller in Ref. [3] during PDAV motions.

Dynamics

The PDAV control problem is studied in a general context; the model used to capture these dynamics is that of a fully actuated rigid body of mass/inertia m and $\mathbf{J}$ connected to a fixed point via a spherical joint by a massless axle of length d. An inertial reference frame $\mathbf{I}_R\{\mathbf{E}_1, \mathbf{E}_2, \mathbf{E}_3\}, \mathbf{E}_i \in \mathbb{R}^3$, and a body fixed frame $\mathbf{I}_b\{\mathbf{b}_1, \mathbf{b}_2, \mathbf{b}_3\}, \mathbf{b}_i \in \mathbb{R}^3$ are defined. Frame $\mathbf{I}_b$ is attached at the center of mass (CoM) of the rotating rigid body and $\mathbf{R}(t) \in \mathrm{SO}(3)$ is the rotation matrix from $\mathbf{I}_b$ to $\mathbf{I}_R$. The angular velocity of the system in $\mathbf{I}_b$ is denoted as ${}^b\boldsymbol{\omega} = [\omega_1, \omega_2, \omega_3]^T$. An element of the two-sphere $\mathbf{q}(t) \in \mathrm{S}^2 = \{\mathbf{q} \in \mathbb{R}^3 | \mathbf{q}^T\mathbf{q} = 1\}$, collinear with the axis of body rotation, $\mathbf{b}_3$, and the component of the angular velocity along $\mathbf{q}(t)$, namely, $\omega_3(t) \in \mathbb{R}$, describe the configuration space of the system with respect to the PDAV task. These are given by

$$\mathbf{q}(t) = \mathbf{R}(t)\mathbf{b}_3, \quad \mathbf{b}_3 = [0, 0, 1]^T \tag{1a}$$

$$\omega_3(t) = \mathbf{b}_3^T {}^b\boldsymbol{\omega}(t) \tag{1b}$$

The attitude equations of motion are

$$\mathbf{J}\,{}^b\dot{\boldsymbol{\omega}} = {}^b\mathbf{u} + {}^b\mathbf{n} - S({}^b\boldsymbol{\omega})\mathbf{J}\,{}^b\boldsymbol{\omega} \tag{2a}$$

$$\dot{\mathbf{R}} = \mathbf{R}S({}^b\boldsymbol{\omega}) \tag{2b}$$

$$\dot{\mathbf{q}} = S(\mathbf{R}\,{}^b\boldsymbol{\omega})\mathbf{q} = \mathbf{R}S({}^b\boldsymbol{\omega})\mathbf{b}_3 \tag{2c}$$

where ${}^b\mathbf{u} = [u_1, u_2, u_3]^T \in \mathbb{R}^3$ is the control moment and ${}^b\mathbf{n}$ contains all other system moments, and depends on the system under

[1]Corresponding author.

Contributed by the Dynamic Systems Division of ASME for publication in the Journal of Dynamic Systems, Measurement, and Control. Manuscript received April 14, 2020; final manuscript received December 6, 2020; published online February 26, 2021. Assoc. Editor: Amit K. Sanyal.

study. The cross product map, $S(.) : \mathbb{R}^3 \to \mathfrak{so}(3)$, and its inverse, $S^{-1}(.) : \mathfrak{so}(3) \to \mathbb{R}^3$, are given in Eq. (A1).

Pointing Direction/Angular Velocity Control System

Before proceeding with the CL analysis, the PDAV controller, Ref. [3], is summarized. For a detailed development, see Refs. [3] and [12]. A sufficiently smooth desired pointing direction, $\mathbf{q}_d$, and angular velocity, ${}^b\boldsymbol{\omega}_d$, are given by

$$\mathbf{q}_d = \mathbf{R}_d(t)\mathbf{b}_3 \in \mathrm{S}^2, \quad {}^b\boldsymbol{\omega}_d = \omega_d(t)\mathbf{b}_3 \tag{3}$$

The angular velocity error vector, ${}^b\mathbf{e}_\omega$, and the attitude error vector, ${}^b\mathbf{e}_q$, are given by [3]

$${}^b\mathbf{e}_\omega({}^b\boldsymbol{\omega}, {}^b\boldsymbol{\omega}_d, \mathbf{R}, \mathbf{R}_d) = {}^b\boldsymbol{\omega} - \mathbf{R}^T\mathbf{R}_d\,{}^b\boldsymbol{\omega}_d \tag{4a}$$

$${}^b\mathbf{e}_q(\mathbf{q}, \mathbf{q}_d, \mathbf{R}) = \mathbf{R}^T S(\mathbf{q}_d)\mathbf{q} \tag{4b}$$

The control law, ${}^b\mathbf{u}$, given in Ref. [3]

$${}^b\mathbf{u} = \eta^{-1}\mathbf{J}(-\eta\,\boldsymbol{\alpha} - (\Lambda + \Psi){}^b\dot{\mathbf{e}}_q - \dot{\Psi}\,{}^b\mathbf{e}_q - \gamma\,\mathbf{s}) - {}^b\mathbf{n} + S({}^b\boldsymbol{\omega})\mathbf{J}\,{}^b\boldsymbol{\omega} \tag{5a}$$

$$\boldsymbol{\alpha} = S({}^b\boldsymbol{\omega})\mathbf{R}^T\mathbf{R}_d\,{}^b\boldsymbol{\omega}_d - \mathbf{R}^T\mathbf{R}_d\,{}^b\dot{\boldsymbol{\omega}}_d \tag{5b}$$

$$\mathbf{s} = (\Lambda + \Psi){}^b\mathbf{e}_q + \eta\,{}^b\mathbf{e}_\omega \tag{5c}$$

$$\Psi = 1 - \mathbf{q}^T\mathbf{q}_d \tag{5d}$$

results in the following CL dynamics:

$${}^b\dot{\boldsymbol{\omega}} = \eta^{-1}(-(\Lambda + \Psi){}^b\dot{\mathbf{e}}_q - \dot{\Psi}\,{}^b\mathbf{e}_q - \gamma\mathbf{s}) - \boldsymbol{\alpha} \tag{6a}$$

$$\dot{\mathbf{q}} = \mathbf{R}S({}^b\boldsymbol{\omega})\mathbf{b}_3 \tag{6b}$$

where the terms $\dot{\Psi}$ and ${}^b\dot{\mathbf{e}}_q$ are given in App. A and $\eta, \gamma, \Lambda \in \mathbb{R}^+$ are control gains. The gains Λ, η, and γ are defined as a function of a response settling time, τ_c, damping ratio, ζ_c, and a constant, $\kappa \in (0, 1]$, as follows:

$$\Lambda = \omega_c^2, \quad \eta = 2\zeta_c\omega_c, \quad \gamma = (1+\kappa)\eta\omega_d^2\Lambda^{-1}$$

$$\omega_c = \begin{cases} 4(\zeta_c\tau_c)^{-1}, & \text{if } 0.2 < \zeta_c \le 0.9 \\ 6(\zeta_c\tau_c)^{-1}, & \text{if } 0.9 < \zeta_c \le 1 \\ 4(\tau_c|-\zeta_c + \sqrt{\zeta_c^2 - 1}|)^{-1}, & \text{if } \zeta_c > 1 \end{cases} \tag{7}$$

It is noted that proof of stability of the control algorithm is prior work provided in Refs. [3] and [12]. Since the controller employs feedback linearization, the CL dynamics given in Eq. (6) are independent of the physical system. The set of CL equilibria, Q_e, is given by

$$Q_e = \{Q_1(\zeta), Q_2(\zeta) | \zeta \in \mathbb{R}\} \tag{8a}$$

$$Q_1(\zeta) = (\exp(\zeta S(\mathbf{R}_d\mathbf{b}_3))\mathbf{R}_d\mathbf{b}_3, {}^b\boldsymbol{\omega}_d) \tag{8b}$$

$$Q_2(\zeta) = (\exp(\pi S(\mathbf{R}_d\mathbf{b}_1))\exp(\zeta S(\mathbf{R}_d\mathbf{b}_3))\mathbf{R}_d\mathbf{b}_3, -{}^b\boldsymbol{\omega}_d) \tag{8c}$$

Via ζ parametrization, Q_e includes all possible configurations. The subset, Q_1, corresponds to the desired equilibrium, i.e., $(\mathbf{q}_e, {}^b\boldsymbol{\omega}_e) = (\mathbf{q}_d, {}^b\boldsymbol{\omega}_d)$, and the second corresponds to the antipodal equilibrium, i.e., $(\mathbf{q}_e, {}^b\boldsymbol{\omega}_e) = (-\mathbf{q}_d, -{}^b\boldsymbol{\omega}_d)$; the desired equilibrium $(\mathbf{q}_d, {}^b\boldsymbol{\omega}_d) \in Q_1$ is almost globally exponentially stable [3,12].

Examples of Applying Pointing Direction/Angular Velocity Control

A smooth PDAV motion is characterized by high frequency precession/nutation oscillations. To demonstrate this, simulation data from two systems are presented.

System (a) describes the dynamics of vectored thrust generation by means of an outrunner motor/propeller assembly (a "fast" system performing PDAV maneuvers in a few seconds with a high spin velocity)

$$\omega_3(t) \approx 600\,[\mathrm{rad/s}], \quad \tau_c = 10^{-3}\,s, \quad \zeta_c = 1, \kappa = 0.05 \tag{9}$$

System (b) describes the dynamics of a spin-stabilized satellite (a "slow" system maneuvering at a scale of a few hundred seconds with a very low spin velocity)

$$\omega_3(t) \approx 0.77\,[\mathrm{rad/s}], \quad \tau_c = 0.9\,s, \quad \zeta_c = 1, \kappa = 0.05 \tag{10}$$

Due to space constraint, further details on these systems are omitted; however, they are not essential for the purpose of this exposition.

The 3D pointing response is shown in Fig. 1(*a*) for system (a), and in Fig. 1(*b*) for system (b), demonstrating smooth precision PDAV tracking. For both systems, the attitude error remains below 4×10^{-3} % and the spin tracking error, ${}^b\mathbf{e}_{\omega_3}$, remains below 8×10^{-3} rad/s (not shown due to space constraint). For system (a), the pointing actuators must generate torques up to 0.1 Nm, see Fig. 1(*e*), while for system (b), the actuators generate torques up to 2 Nm, see Fig. 1(*f*). However, the appearance of high-frequency gyroscopic oscillations, shown in Fig. 1(*c*) for system (a), and in Fig. 1(*d*) for system (b) (top and middle rows), identified via the "313" Euler sequence [25] as precession (variation of the first Euler angle ϕ), and nutation (variation of the second Euler angle θ), are of critical significance. Applying FFT on the precession/nutation responses of Figs. 1(*c*) and 1(*d*) shows oscillations of 190.98 Hz (system (a)) and oscillations 0.244 Hz (system (b)).

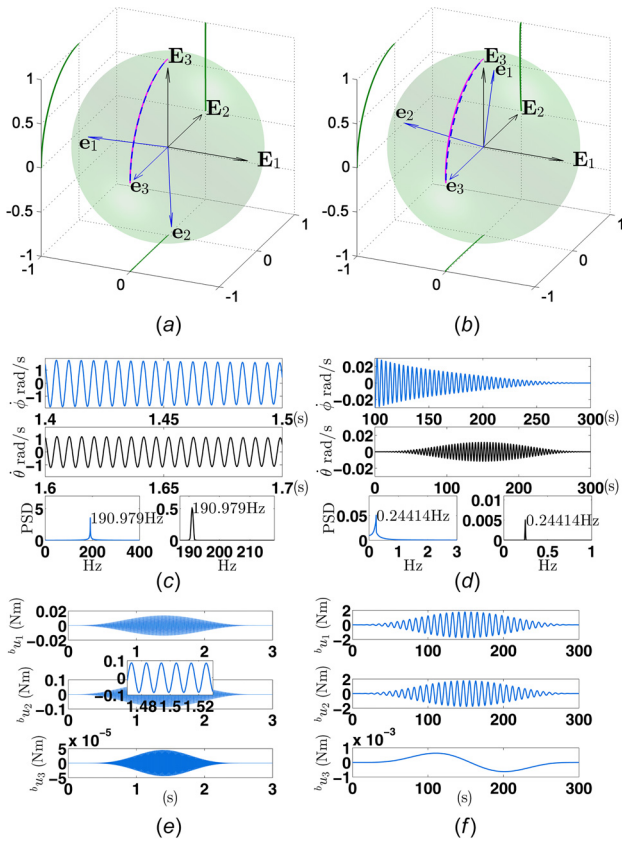

Fig. 1 PDAV simulations of steady spin velocity. System (*a*), Figs. (1(*a*), 1(*c*), and 1(*e*)). System (*b*), Figs. (1(*b*), 1(*d*), and 1(*f*)). Figures (1(*a*) and 1(*b*)) Pointing maneuver including plane projections. Figures (1(*c*) and 1(*d*)) Oscillation response. Top: precession, $\dot{\phi}$. Middle: nutation, $\dot{\theta}$. Bottom left: Fast Fourier transform (FFT) precession frequency. Bottom right: FFT nutation frequency. Figures (1(*e*) and 1(*f*)) Control effort.

These high-frequency precession/nutation oscillations must be taken into account since they have implications on actuator demands and are a source of vibration.

Geometrically Exact Linearization

Next, a coordinate-free, global, geometrically exact linearization of the CL dynamics about a dynamically feasible time-varying trajectory $(\mathbf{q}(t),{}^b\boldsymbol{\omega}(t))$ is derived. To obtain a geometrically exact linearization, it must be ensured that the perturbation of the states still belongs to the configuration manifold [7,24,26,27]. The perturbed states, $(\mathbf{q}(t,\epsilon),{}^b\boldsymbol{\omega}(t,\epsilon))$, are calculated as a function of a variation parameter, $\epsilon \in \mathbb{R}$, via the exponential map, Eq. (A3), as

$$\mathbf{q}(t,\epsilon) = \boldsymbol{\Delta}\mathbf{R}\,\mathbf{q}(t) \tag{11a}$$

$${}^b\boldsymbol{\omega}(t,\epsilon) = {}^b\boldsymbol{\omega}(t) + \epsilon\delta\mathbf{w}(t) \tag{11b}$$

$$\mathbf{R}(t,\epsilon) = \boldsymbol{\Delta}\mathbf{R}\,\mathbf{R}(t) \tag{11c}$$

$$\boldsymbol{\Delta}\mathbf{R} = \exp(\epsilon S(\boldsymbol{\xi}(t))) \tag{11d}$$

with the instantaneous axis of rotation, $\boldsymbol{\xi}(t)$, to belong to the tangent space, $T_q\mathrm{S}^2 = \{\boldsymbol{\xi}(t) \in \mathbb{R}^3 | \mathbf{q}(t)^T\boldsymbol{\xi}(t) = 0\}$, and the curve $\delta\mathbf{w}(t) \in \mathbb{R}^3$. This preserves the geometrical exactness of the perturbed state since $\mathbf{q}(t,\epsilon) \in \mathrm{S}^2$ [7].

Lemma 1. *The derived symbolic variation-based linearization of Eq. (6) about a time-varying trajectory, $(\mathbf{q}(t),{}^b\boldsymbol{\omega}(t))$, is given by*

$$\dot{\mathbf{x}}(t) = \mathbf{A}(t)\mathbf{x}(t) = \begin{bmatrix} \boldsymbol{\Xi}_\xi & \boldsymbol{\Xi}_\omega \\ \boldsymbol{\Omega}_\xi & \boldsymbol{\Omega}_\omega \end{bmatrix} \begin{bmatrix} \boldsymbol{\xi} \\ \delta{}^b\boldsymbol{\omega} \end{bmatrix} \tag{12a}$$

$$\mathbf{C}(t)\mathbf{x}(t) = \begin{bmatrix} \mathbf{q}^T & 0_{1\times3} \end{bmatrix} \begin{bmatrix} \boldsymbol{\xi} \\ \delta{}^b\boldsymbol{\omega} \end{bmatrix} = 0 \tag{12b}$$

where the block matrices $\boldsymbol{\Xi}_\xi, \boldsymbol{\Xi}_\omega, \boldsymbol{\Omega}_\xi, \boldsymbol{\Omega}_\omega \in \mathbb{R}^{3\times3}$ are

$$\boldsymbol{\Xi}_\xi = \mathbf{q}\mathbf{q}^T S(\mathbf{R}^b\boldsymbol{\omega}), \quad \boldsymbol{\Xi}_\omega = (\mathbf{I} - \mathbf{q}\mathbf{q}^T)\mathbf{R} \tag{13a}$$

$$\begin{aligned}
\boldsymbol{\Omega}_\xi = {}& \mathbf{R}^T S(\mathbf{R}_d{}^b\dot{\boldsymbol{\omega}}_d) - S({}^b\boldsymbol{\omega})\mathbf{R}^T S(\mathbf{R}_d{}^b\boldsymbol{\omega}_d) \\
& - \eta^{-1}\{{}^b\mathbf{e}_q(\mathbf{R}^b\mathbf{e}_\omega)^T S(\mathbf{R}^b\mathbf{e}_q) \\
& + {}^b\mathbf{e}_q(\mathbf{R}^b\mathbf{e}_q)^T S(\mathbf{R}^b\mathbf{e}_\omega) + {}^b\dot{\mathbf{e}}_q\mathbf{q}_d^T S(\mathbf{q}) \\
& + (\Lambda + \Psi)(\mathbf{R}^T S(S(\dot{\mathbf{q}}_d)\mathbf{q} + S(\mathbf{q}_d)\dot{\mathbf{q}}) \\
& - \mathbf{R}^T S(\mathbf{q}_d)S(\mathbf{R}S({}^b\boldsymbol{\omega})\mathbf{b}_3) - \mathbf{R}^T S(\dot{\mathbf{q}}_d)S(\mathbf{q}) \\
& - S({}^b\boldsymbol{\omega})\mathbf{R}^T(S(S(\mathbf{q}_d)\mathbf{q}) - S(\mathbf{q}_d)S(\mathbf{q}))) \\
& + ({}^b\mathbf{e}_q(\mathbf{R}^b\mathbf{e}_\omega)^T\mathbf{R} + (\dot{\Psi} + \gamma(\Lambda + \Psi))\mathbf{I})\cdot \\
& \mathbf{R}^T(S(S(\mathbf{q}_d)\mathbf{q}) - S(\mathbf{q}_d)S(\mathbf{q})) + \gamma{}^b\mathbf{e}_q\mathbf{q}_d^T S(\mathbf{q}) \\
& - ({}^b\mathbf{e}_q(\mathbf{R}^b\mathbf{e}_q)^T\mathbf{R} + \eta\gamma\mathbf{I})\mathbf{R}^T S(\mathbf{R}_d{}^b\boldsymbol{\omega}_d)\}
\end{aligned} \tag{13b}$$

$$\begin{aligned}
\boldsymbol{\Omega}_\omega = {}& S(\mathbf{R}^T\mathbf{R}_d{}^b\boldsymbol{\omega}_d) - \eta^{-1}\{({}^b\mathbf{e}_q(\mathbf{R}^b\mathbf{e}_q)^T\mathbf{R} + \eta\gamma\mathbf{I}) \\
& + (\Lambda + \Psi)(S({}^b\mathbf{e}_q) - S(\mathbf{R}^T\mathbf{q}_d)S(\mathbf{b}_3))\}
\end{aligned} \tag{13c}$$

Proof. The infinitesimal variation of the pointing state, $\delta\mathbf{q}(t)$, and the variation of the angular velocity state, $\delta{}^b\boldsymbol{\omega}(t)$, about $(\mathbf{q}(t),{}^b\boldsymbol{\omega}(t))$ are found via Eq. (11), as

$$\delta\mathbf{q}(t) = \frac{d}{d\epsilon}\mathbf{q}(t,\epsilon)\bigg|_{\epsilon=0} = S(\boldsymbol{\xi}(t))\mathbf{q}(t) \tag{14a}$$

$$\delta{}^b\boldsymbol{\omega}(t) = \frac{d}{d\epsilon}{}^b\boldsymbol{\omega}(t,\epsilon)\bigg|_{\epsilon=0} = \delta\mathbf{w}(t) \tag{14b}$$

To obtain a coordinate-free form of Eq. (6b), differentiate first Eq. (14a). This yields

$$\delta\dot{\mathbf{q}}(t) = S(\dot{\boldsymbol{\xi}}(t))\mathbf{q}(t) + S(\boldsymbol{\xi}(t))\dot{\mathbf{q}}(t) \tag{15}$$

Substitution of Eqs. (11) in (6b) followed by differentiation with respect to ϵ, and setting $\epsilon = 0$ results in:

$$\begin{aligned}
\delta\dot{\mathbf{q}}(t) = {}& S(\boldsymbol{\xi}(t))(S(\mathbf{R}(t){}^b\boldsymbol{\omega}(t))\mathbf{q}(t)) \\
& + S(\mathbf{R}(t)\delta\mathbf{w}(t))\mathbf{q}(t)
\end{aligned} \tag{16}$$

Equating Eq. (15) with Eq. (16), and substituting Eq. (6b) yields

$$S(\dot{\boldsymbol{\xi}}(t))\mathbf{q}(t) = S(\mathbf{R}(t)\delta\mathbf{w}(t))\mathbf{q}(t) \tag{17}$$

Equation (17) is to be solved with respect to $\dot{\boldsymbol{\xi}}(t)$. Due to the action of the cross product map on $\mathbf{q}(t)$, both left-side and right-side terms are perpendicular to $\mathbf{q}(t)$. Thus, it holds that

$$S(\mathbf{q}(t))(S(\dot{\boldsymbol{\xi}}(t))\mathbf{q}(t)) = S(\mathbf{q}(t))(S(\mathbf{R}(t)\delta\mathbf{w}(t))\mathbf{q}(t)) \tag{18}$$

Employing the vector triple product identity (Eq. (A2c)) and $\mathbf{q}(t)^T\mathbf{q}(t) = 1$ on Eq. (18), after rearranging

$$\dot{\boldsymbol{\xi}}(t) - (\mathbf{q}(t)^T\dot{\boldsymbol{\xi}}(t))\mathbf{q}(t) = S(\mathbf{q}(t))(S(\mathbf{R}(t)\delta\mathbf{w}(t))\mathbf{q}(t)) \tag{19}$$

Since $\boldsymbol{\xi}(t) \in T_q\mathrm{S}^2$, i.e., $\boldsymbol{\xi}(t)^T\mathbf{q}(t) = 0, \forall t$ then

$$\dot{\boldsymbol{\xi}}(t)^T\mathbf{q}(t) = -\boldsymbol{\xi}(t)^T\dot{\mathbf{q}}(t) \tag{20}$$

and by applying Eqs. (20) to (19), together with Eq. (2c), Eq. (14b) and rearranging terms

$$\begin{aligned}
\dot{\boldsymbol{\xi}}(t) = {}& (-\boldsymbol{\xi}(t)^T S(\mathbf{R}(t){}^b\boldsymbol{\omega}(t))\mathbf{q}(t))\mathbf{q}(t) \\
& + S(\mathbf{q}(t))(S(\mathbf{R}(t)\delta{}^b\boldsymbol{\omega}(t))\mathbf{q}(t))
\end{aligned} \tag{21}$$

Employing Eq. (A2b), on the first term of Eq. (21), and the vector triple product identity (Eq. (A2c)) on the second term of Eq. (21), the linearized equation of motion of Eq. (6b) is obtained. It is given by

$$\begin{aligned}
\dot{\boldsymbol{\xi}}(t) = {}& \mathbf{q}(t)\mathbf{q}(t)^T S(\mathbf{R}(t)^b\boldsymbol{\omega}(t))\boldsymbol{\xi}(t) \\
& + (\mathbf{I} - \mathbf{q}(t)\mathbf{q}(t)^T)\mathbf{R}(t)\delta{}^b\boldsymbol{\omega}(t)
\end{aligned} \tag{22}$$

In the same manner using Eq. (11) in Eq. (6a), differentiating with respect to ϵ, setting $\epsilon = 0$, and after considerable manipulations, the linearized equation of motion of Eq. (6a) is obtained; the derived symbolic variation-based linearization of Eq. (6) about a time-varying trajectory, $(\mathbf{q}(t),{}^b\boldsymbol{\omega}(t))$, is given by Eq. (12).

Note that Eq. (12) corresponds to a constrained, implicitly time-varying linear system that is valid globally. ■

Lemma 2. *The nullspace of Eq. (12b), $\mathcal{N}(\mathbf{C})$, is given by the column-span of matrix $\mathbf{N}$ and its orthogonal complement, $\mathcal{N}(\mathbf{C})^\perp$, by the column span of $\mathbf{N}^\perp$, where*

$$\mathbf{N} = \begin{bmatrix} \mathbf{0}_{3\times1} & \mathbf{0}_{3\times1} & \mathbf{0}_{3\times1} & \mathbf{q}^\perp & S(\mathbf{q})\mathbf{q}^\perp \\ \mathbf{q}^\perp & S(\mathbf{q})\mathbf{q}^\perp & \mathbf{q} & \mathbf{0}_{3\times1} & \mathbf{0}_{3\times1} \end{bmatrix} \tag{23a}$$

$$\mathbf{N}^\perp = \begin{bmatrix} \mathbf{q} \\ \mathbf{0}_{3\times1} \end{bmatrix} \tag{23b}$$

Proof. The fact that $\mathbf{C}\mathbf{N} = 0$, $\mathbf{C}\mathbf{N}^\perp \neq 0$, and $\mathbf{N}^T\mathbf{N}^\perp = 0$ verifies the claim. Note that $\mathrm{colspan}\{[\mathbf{N}\,\mathbf{N}^\perp]\} = \mathbb{R}^6$. ■

Lemma 3. *The constrained space of Eq. (12a) is time invariant, i.e., $d/dt(\mathbf{C}(t)\mathbf{x}(t)) \equiv 0$.*

Proof. Differentiating Eq. (12b) yields

$$\frac{d}{dt}(\mathbf{C}\mathbf{x}) = (\mathbf{C}\mathbf{A} + \dot{\mathbf{C}})\mathbf{x} \tag{24a}$$

$$= \mathbf{q}^T S(\mathbf{R}^b\boldsymbol{\omega})\boldsymbol{\xi} + \mathbf{q}^T S(\mathbf{R}^b\boldsymbol{\omega})^T\boldsymbol{\xi} = 0 \tag{24b}$$

This implies that if the initial condition satisfies $\mathbf{C}(t_0)\mathbf{x}(t_0) = 0$, the value $\mathbf{C}(t)\mathbf{x}(t)$ is conserved $\forall t$.

Thus, if the initial condition starts in the constraint space, the system trajectory remains in the constrained space. Next, the local stabilization properties of the linearized dynamics in the neighborhood of its equilibria are analyzed. ■

Equilibrium Eigenstructure Analysis

Next, by inserting into matrix $\mathbf{A}$ of Eq. (12*a*), PDAV equilibria that belong to the desired set, Q_1, and to the antipodal set, Q_2, their eigenstructure (i.e., eigenvalues/eigenvectors) is analyzed, yielding results of general nature. A generic PDAV command is given by

$$\mathbf{q}_d = \mathbf{R}_d\mathbf{b}_3, \quad \mathbf{R}_d = \mathbf{I}, \quad {}^b\boldsymbol{\omega}_d = \omega_d\mathbf{b}_3, \quad {}^b\dot{\boldsymbol{\omega}}_d = \mathbf{0} \tag{25}$$

where the spin velocity $\omega_d \in \mathbb{R}$ and the controller gains remain unspecified. The desired PDAV command via Eq. (8) yields two equilibrium solutions

$$(\mathbf{q}_e, {}^b\boldsymbol{\omega}_e) = (\mathbf{b}_3, \omega_d\mathbf{b}_3) \in Q_1 \tag{26a}$$

$$(\mathbf{q}_e, {}^b\boldsymbol{\omega}_e) = (-\mathbf{b}_3, -\omega_d\mathbf{b}_3) \in Q_2 \tag{26b}$$

Corresponding to the desired and the antipodal equilibrium, respectively. Calculating the eigenstructure of matrix $\mathbf{A}$, i.e., its eigenvalues, $\lambda_{i=1,\ldots,6}$, and eigenvectors, $\mathbf{v}_{i=1,\ldots,6}$ at these two equilibria allows the analysis of the systems local behavior.

Desired Equilibrium

PROPOSITION 1. *For a gain γ such that*

$$\gamma > \eta\omega_d^2\Lambda^{-1} \tag{27}$$

the equilibrium, $(\mathbf{q}_e, {}^b\boldsymbol{\omega}_e) \in Q_1$, given in Eq. (26a) is an asymptotically stable focus, i.e.,

$$\mathrm{Re}[\lambda_{2,6}] < \lambda_4 < \mathrm{Re}[\lambda_{1,5}] < 0 \tag{28}$$

The eigenstructure of the desired equilibrium, Q_1, is

$$\begin{aligned}
\lambda_1 &= \left(-\left(\frac{\gamma}{2}+\frac{\Lambda}{2\eta}\right)+c\right)+\left(\frac{\omega_d}{2}+d\right)i \\
\mathbf{v}_1 &\in \ \mathrm{colspan}\{\mathbf{e}_1,\mathbf{e}_2,\mathbf{e}_4,\mathbf{e}_5\} \\
\lambda_2 &= \left(-\left(\frac{\gamma}{2}+\frac{\Lambda}{2\eta}\right)-c\right)-\left(\frac{\omega_d}{2}+d\right)i \\
\mathbf{v}_2 &\in \ \mathrm{colspan}\{\mathbf{e}_1,\mathbf{e}_2,\mathbf{e}_4,\mathbf{e}_5\} \\
\lambda_3 &= 0, \quad \mathbf{v}_3 = \mathbf{e}_3, \quad \lambda_4 = -\gamma, \quad \mathbf{v}_4 = \mathbf{e}_6 \\
\lambda_5 &= \bar{\lambda}_1, \quad \mathbf{v}_5 = \bar{\mathbf{v}}_1, \quad \lambda_6 = \bar{\lambda}_2, \quad \mathbf{v}_6 = \bar{\mathbf{v}}_2
\end{aligned} \tag{29}$$

where the overbar denotes the complex conjugate operation and the vector $\mathbf{e}_i \in \mathbb{R}^6$ denotes the ith Euclidean basis element. The constants $c, d \in \mathbb{R}$ are given by

$$c = \sqrt{\frac{a+\sqrt{a^2+b^2}}{2}}, \quad d = \sqrt{\frac{-a+\sqrt{a^2+b^2}}{2}} \tag{30}$$

and the constants $a, b \in \mathbb{R}$ are given by

$$a = \frac{(\eta\gamma-\Lambda)^2}{4\eta^2}+\frac{3\omega_d^2}{4}, \quad b = \frac{\omega_d}{2}\left(\gamma+\frac{\Lambda}{\eta}\right)$$

Proof. Substituting Eq. (26*a*) in Eq. (12*a*) results in

$$\mathbf{A} = \begin{bmatrix} \mathbf{0}_{2\times2} & \mathbf{0}_{2\times1} & \mathbf{I}_{2\times2} & \mathbf{0}_{2\times1} \\ \mathbf{0}_{1\times2} & \mathbf{0} & \mathbf{0}_{1\times2} & \mathbf{0} \\ \mathbf{A}_1 & \mathbf{0}_{2\times1} & \mathbf{A}_2 & \mathbf{0}_{2\times1} \\ \mathbf{0}_{1\times2} & \mathbf{0} & \mathbf{0}_{1\times2} & -\gamma \end{bmatrix} \tag{31}$$

where the matrices $\mathbf{A}_1, \mathbf{A}_2 \in \mathbb{R}^{2\times2}$ are given by

$$\mathbf{A}_1 = \begin{bmatrix} \omega_d^2-\dfrac{\gamma\Lambda}{\eta} & -\omega_d\left(\gamma+\dfrac{\Lambda}{\eta}\right) \\ \omega_d\left(\gamma+\dfrac{\Lambda}{\eta}\right) & \omega_d^2-\dfrac{\gamma\Lambda}{\eta} \end{bmatrix},$$

$$\mathbf{A}_2 = \begin{bmatrix} -\dfrac{\Lambda}{\eta}-\gamma & -\omega_d \\ \omega_d & -\dfrac{\Lambda}{\eta}-\gamma \end{bmatrix}$$

Using a symbolic calculation software, Eq. (31) yields the eigenstructure given in Eq. (29).

Inspecting the eigenvalues, λ_1, λ_5, in Eq. (29), it is observed that a sufficiently large γ gain is needed to yield negative λ_1, λ_5. The gains Λ, η are not considered as means to modify the eigenvalues because they define the nonlinear surface, $\mathbf{s}$, which acts as a proportional-derivative (PD) correction term. To find the range of γ, the real component of λ_1 is set to zero and then manipulated accordingly (by squaring twice) to obtain the following cubic equation:

$$\Lambda\eta^{-1}(\gamma-\eta\omega_d^2\Lambda^{-1})(\gamma+\Lambda\eta^{-1})^2 = 0 \tag{32}$$

This equality implies that for a gain γ according to Eq. (27), then $\mathrm{Re}[\lambda_{1,5}] < 0$ and hence Eq. (28) holds. ■

Antipodal Equilibrium

PROPOSITION 2. *$\forall\gamma \in \mathbb{R}^+$, the equilibrium, $(\mathbf{q}_e, {}^b\boldsymbol{\omega}_e) \in Q_2$, given in Eq. (26b) is a saddle point, i.e.,*

$$\mathrm{Re}[\lambda_{1,5}] < \lambda_4 < 0 < \mathrm{Re}[\lambda_{2,6}] \tag{33}$$

The eigenstructure of the antipodal equilibrium, Q_2, is

$$\begin{aligned}
\lambda_1 &= \left(-\frac{\gamma}{2}+\left(\frac{\Lambda}{2\eta}+\frac{1}{\eta}\right)-c_r\right)+\left(\frac{\omega_d}{2}-d_r\right)i \\
\mathbf{v}_1 &\in \ \mathrm{colspan}\{\mathbf{e}_1,\mathbf{e}_2,\mathbf{e}_4,\mathbf{e}_5\} \\
\lambda_2 &= \left(-\frac{\gamma}{2}+\left(\frac{\Lambda}{2\eta}+\frac{1}{\eta}\right)+c_r\right)+\left(\frac{\omega_d}{2}+d_r\right)i \\
\mathbf{v}_2 &\in \ \mathrm{colspan}\{\mathbf{e}_1,\mathbf{e}_2,\mathbf{e}_4,\mathbf{e}_5\} \\
\lambda_3 &= 0, \quad \mathbf{v}_3 = \mathbf{e}_3, \quad \lambda_4 = -\gamma, \quad \mathbf{v}_4 = \mathbf{e}_6 \\
\lambda_5 &= \bar{\lambda}_1, \quad \mathbf{v}_5 = \bar{\mathbf{v}}_1, \quad \lambda_6 = \bar{\lambda}_2, \quad \mathbf{v}_6 = \bar{\mathbf{v}}_2
\end{aligned} \tag{34}$$

where the constants $c_r, d_r \in \mathbb{R}$ are given by

$$c_r = \sqrt{\frac{a_r+\sqrt{a_r^2+b_r^2}}{2}}, \quad d_r = \sqrt{\frac{-a_r+\sqrt{a_r^2+b_r^2}}{2}} \tag{35}$$

and the constants $a_r, b_r \in \mathbb{R}$ are given by

$$a_r = \frac{(\eta\gamma+\Lambda)^2}{4\eta^2}+\frac{\Lambda+\eta\gamma+1}{\eta^2}+\frac{3\omega_d^2}{4}$$

$$b_r = \left(\frac{\omega_d\gamma}{2}-\frac{\omega_d\Lambda}{2\eta}-\frac{\omega_d}{\eta}\right)$$

Proof. Employing Eq. (26*b*) in Eq. (12*a*) results in

$$\mathbf{A} = \begin{bmatrix} \mathbf{0}_{2\times2} & \mathbf{0}_{2\times1} & \mathbf{A}_1 & \mathbf{0}_{2\times1} \\ \mathbf{0}_{1\times2} & \mathbf{0} & \mathbf{0}_{1\times2} & \mathbf{0} \\ \mathbf{A}_2 & \mathbf{0}_{2\times1} & \mathbf{A}_3 & \mathbf{0}_{2\times1} \\ \mathbf{0}_{1\times2} & \mathbf{0} & \mathbf{0}_{1\times2} & -\gamma \end{bmatrix} \tag{36}$$

where the matrices $\mathbf{A}_1, \mathbf{A}_2, \mathbf{A}_3 \in \mathbb{R}^{2\times 2}$ are given by

$$\mathbf{A}_1 = \begin{bmatrix} -1 & 0 \\ 0 & 1 \end{bmatrix}, \quad \mathbf{A}_2 = \begin{bmatrix} -\omega_d^2 - \dfrac{\gamma(\Lambda+2)}{\eta} & -\omega_d\left(\dfrac{\Lambda+2}{\eta} - \gamma\right) \\ -\omega_d\left(\dfrac{\Lambda+2}{\eta} - \gamma\right) & \omega_d^2 + \dfrac{\gamma(\Lambda+2)}{\eta} \end{bmatrix}$$

$$\mathbf{A}_3 = \begin{bmatrix} \dfrac{\Lambda+2}{\eta} - \gamma & \omega_d \\ -\omega_d & \dfrac{\Lambda+2}{\eta} - \gamma \end{bmatrix}$$

Via a symbolic calculation software, Eq. (36) yields the eigenstructure given in Eq. (34).

To find how the gain γ influences the eigenvalues, the real component of λ_1 is set to zero and then manipulated accordingly (by squaring twice). This yields the cubic

$$\frac{-\Lambda-2}{\eta}\left(\gamma + \frac{\eta\omega_d^2}{\Lambda+2}\right)\left(\gamma - \frac{\Lambda+2}{\eta}\right)^2 = 0 \tag{37}$$

Any gain $\gamma > -\eta\omega_d^2/(\Lambda+2)$ yields $\mathrm{Re}[\lambda_1] < 0$. Using a similar analysis, it can be shown that $\mathrm{Re}[\lambda_2] > 0, \forall\gamma \in \mathbb{R}^+$ proving Eq. (33). ■

Local Solution. Using Lemma 2, the nullspace base, $\mathcal{N}(\mathbf{C})$, of Eq. (12*b*) for both equilibria is computed to be

$$\mathcal{N}(\mathbf{C}) = \mathrm{colspan}\{\mathbf{e}_1, \mathbf{e}_2, \mathbf{e}_4, \mathbf{e}_5, \mathbf{e}_6\} \tag{38}$$

The local solution, $\mathbf{x}(t)$, of Eq. (12*a*) is given by [28]

$$\mathbf{x}(t) = \sum_{k=3}^{4} a_k e^{\lambda_k t}\mathbf{v}_k + \sum_{k=1}^{2}\left(c_k e^{\lambda_k t}\mathbf{v}_k + \bar{c}_k e^{\bar{\lambda}_k t}\bar{\mathbf{v}}_k\right) \tag{39}$$

where $a_{k=3,4} \in \mathbb{R}, c_{k=1,2} \in \mathbb{C}$. For both equilibria, it is observed that $\mathbf{v}_3 \notin \mathcal{N}(\mathbf{C})$. Thus, $\mathbf{v}_3$ violates the topological constraint of Eq. (12*b*). As a consequence, for all $\mathbf{x}(t_0)$ that comply with Eq. (12*b*), $a_3 = 0$, meaning that eigenvalue, λ_3, does not participate in the local solution.

Precession/Nutation Frequency Estimation

The investigation conducted earlier on PDAV control examples revealed that a smooth PDAV motion is accompanied by high frequency gyroscopic nutation/precession oscillations (see Figs. 1(*c*) and 1(*d*) (top and middle rows)). These high frequency oscillations reveal that to achieve smooth PDAV motion, competent actuators are required, to compensate for the oscillations. Next, a method for quickly obtaining estimates of the frequency of the gyroscopic nutation/precession oscillations during PDAV motion is derived.

State-Constrained Controllability of an Arbitrary Pointing Direction/Angular Velocity Control System

To analytically investigate the PDAV tracking motion, the state-constrained controllability properties of an arbitrary PDAV system in the neighborhood of a time-varying desired trajectory are identified. This is done next following the method proposed in Ref. [27].

The dynamics of an arbitrary PDAV system are given by Eq. (2) after setting ${}^b\mathbf{n} = 0$. Equating the perturbed time-varying trajectory in Eqs. (11) and (11*b*), with a desired time-varying trajectory (i.e., $\mathbf{q}(t,\epsilon) = \exp(\epsilon S(\boldsymbol{\xi}(t)))\mathbf{q}_d(t)$ and do the same for the perturbed time-varying angular velocity) followed by calculating the variation-based linearization, the result is:

$$\dot{\mathbf{x}} = \mathbf{A}_d(t)\mathbf{x} + \mathbf{B}\delta^b\mathbf{u} \tag{40a}$$

$$\mathbf{C}_d(t)\mathbf{x} = 0 \tag{40b}$$

where the matrices $\mathbf{A}_d(t), \mathbf{B}, \mathbf{C}_d(t)$ are given by

$$\mathbf{A}_d(t) = \begin{bmatrix} \mathbf{q}_d\mathbf{q}_d^T S(\mathbf{R}_d{}^b\boldsymbol{\omega}_d) & (\mathbf{I} - \mathbf{q}_d\mathbf{q}_d^T)\mathbf{R}_d \\ \mathbf{0}_{3\times 3} & \mathbf{J}^{-1}(S(\mathbf{J}^b\boldsymbol{\omega}_d) - S({}^b\boldsymbol{\omega}_d)\mathbf{J}) \end{bmatrix} \tag{41}$$

$$\mathbf{C}_d(t) = [\mathbf{q}_d^T \quad \mathbf{0}_{1\times 3}], \quad \mathbf{B} = [\mathbf{0}_{3\times 3} \quad \mathbf{I}]^T$$

Proposition 3. *The linear time-varying system, Eq. (40), obtained as the linearization of an arbitrary PDAV system about a time-varying desired trajectory, is controllable for all dynamically feasible desired trajectories.*

Proof. This is showed by adapting Lemmas 1 and 3 from Ref. [27] to this system using the fact that $d/dt(\mathbf{C}_d(t)\mathbf{x}(t)) \equiv 0$, the fact that the nullspace of the constraint matrix, $\mathbf{C}_d$, is given by the column span of Eq. (23*a*) and that the controllable subspace, $\mathcal{R}([\mathbf{B}\ \mathscr{A}\ \mathbf{B}])$, covers the constraint space. Note that $\mathcal{R}(.)$ indicates the range, $\mathscr{A}^k = (d/dt + \mathbf{A}_d(t))^k$ is the linear operator [29], and the controllability matrix [30], $[\mathbf{B}, \mathscr{A}\ \mathbf{B}]$, is derived as

$$[\mathbf{B}\ \mathscr{A}\ \mathbf{B}] = \begin{bmatrix} \mathbf{0}_{3\times 3} & (\mathbf{I} - \mathbf{q}_d\mathbf{q}_d^T)\mathbf{R}_d \\ \mathbf{I} & \mathbf{J}^{-1}(S(\mathbf{J}^b\boldsymbol{\omega}_d) - S({}^b\boldsymbol{\omega}_d)\mathbf{J}) \end{bmatrix} \tag{42}$$

Proposition 3 implies that the origin is reachable by any dynamically feasible system state and the geometrically exact linearization of an arbitrary PDAV system is controllable under state constraints. Similarly, since the constraint space of the CL system is time invariant (see Eq. (24)) and because the eigenstructure of the desired equilibrium, Eq. (29), covers the constraint space, Eq. (23*a*), the trajectory tracking process can be used in the frequency estimation methodology.

In a CL system performing trajectory tracking, the system states at the beginning of the motion are at an equilibrium corresponding to a user-desired system state. Via the smooth and slow shift of the desired PDAV command (as instructed by the smooth desired trajectory), the system equilibrium changes to a new desired state due to the action of the controller. As a consequence, the system states continually track the varying desired PDAV command. Hence, CL smooth trajectory tracking can be considered as a continuous chain/sequence of infinitesimal flows (solutions) following an infinitesimally varying desired PDAV command. This reasoning allows the assumption that in the neighborhood of the desired equilibrium (dictated by a sufficiently smooth time-varying trajectory), an accurate estimate of the frequency of the gyroscopic oscillations can be acquired via Eq. (39), i.e., the local solution, $\mathbf{x}(t)$, of the linearized system. The validity of this assumption is supported by the developments of Proposition 3, and this rationale directs the development of the method. The derivation is given next.

The frequency estimate is based on the local solution, $\mathbf{x}(t)$, in the neighborhood of the desired equilibrium, given in Eq. (26*a*). Using the fact that $a_3 = 0$ and by omitting λ_2 because $\mathrm{Re}[\lambda_2] \lll \mathrm{Re}[\lambda_1]$, the eigenstructure given in Eq. (29) is employed in Eq. (39). After some manipulations, the following is obtained:

$$\begin{aligned}\mathbf{x}(t) = a_4 e^{\lambda_4 t}\mathbf{e}_6 + 2\{&\mathrm{Re}[c_1](\cos(\mu_1 t)\mathrm{Re}[\mathbf{v}_1] \\ &- \sin(\mu_1 t)\mathrm{Im}[\mathbf{v}_1]) - \mathrm{Im}[c_1](\cos(\mu_1 t)\mathrm{Im}[\mathbf{v}_1] \\ &+ \sin(\mu_1 t)\mathrm{Re}[\mathbf{v}_1])\}\end{aligned} \tag{43}$$

where $\mu_k = \mathrm{Im}[\lambda_k]$.

The rotational velocity response, ${}^b\boldsymbol{\omega}$, in the neighborhood of the equilibrium is captured by the last three components of the local solution vector, $\mathbf{x}(t)$, see Eq. (12*a*). To identify the precession rate, $\dot{\phi}$, and nutation rate, $\dot{\theta}$, with the system rotational velocity, ${}^b\boldsymbol{\omega}$, via the "313" Euler sequence we have

$$\begin{bmatrix}\dot{\phi}\\ \dot{\theta}\\ \dot{\psi}\end{bmatrix}=\begin{bmatrix}\dfrac{\sin(\psi)}{\sin(\theta)} & \dfrac{\cos(\psi)}{\sin(\theta)} & 0\\ \cos(\psi) & -\sin(\psi) & 0\\ -\dfrac{\sin(\psi)\cos(\theta)}{\sin(\theta)} & -\dfrac{\cos(\psi)\cos(\theta)}{\sin(\theta)} & 1\end{bmatrix}\begin{bmatrix}\omega_1\\ \omega_2\\ \omega_3\end{bmatrix} \tag{44}$$

The third Euler angle, ψ, is the rotation angle of the rotating body about its body-fixed axis $\mathbf{b}_3$. Notice that by aligning the third axis, $\mathbf{E}_3$, of the inertial frame with the desired pointing axis, $\mathbf{q}_d$, the precession rate, $\dot{\phi}$, given by Eq. (44), holds only when $\theta \notin \{0, k\pi | k \in \mathbb{Z}\}$, i.e., the axis of rotation of the first Euler angle, ϕ, is not aligned with the axis of rotation of the third Euler angle, ψ. This agrees with the physical intuition that no precession exists when the motor axis is aligned with the desired pointing axis because the system is already at one of the two equilibrium points. To find frequency estimates for the precession and nutation rates, $\dot{\phi}$, $\dot{\theta}$, an approximation of $\psi(t)$ is needed.

Spinning Angle Approximation. The sixth component of the local solution vector, $\mathbf{x}(t)$, via Eq. (43) equals to

$$\mathbf{x}^T(t)\,\mathbf{e}_6 = \delta\omega_3 = a_4 e^{\lambda_4 t} = a_4 e^{-\gamma t} \tag{45}$$

Gain γ needs to comply to Eq. (27) to ensure stability. As a result, irrespective of the system, the time constant ($\tau = \gamma^{-1}$ s) in Eq. (45) is always very small with respect to the CL dynamics. This fact, combined with Eq. (11*b*), signifies that "close" to the desired equilibrium, it holds that

$$\omega_3 \approx \omega_d \tag{46}$$

i.e., in the neighborhood of the desired equilibrium, the spinning angle speed converges very quickly to the desired value, ω_d. Also, via Eq. (44), the following holds:

$$\omega_3 = \dot{\psi} + \dot{\phi}\cos(\theta) \tag{47}$$

Because $\dot{\psi} \gg\gg \dot{\phi}$, the term $\dot{\phi}\cos(\theta)$ is neglected. Combining Eqs. (46) and (47) leads to $\dot{\psi} \approx \omega_d$. Hence, in the neighborhood of the equilibrium the spinning angle, $\psi(t)$, can be approximated by

$$\psi(t) \approx \omega_3 t + \psi(t_0) = \omega_d t + \psi_0 \tag{48}$$

Nutation (Precession) Frequency Estimation

Employing the spinning angle approximation, Eq. (48), into the local solution, Eq. (43), the components of the local solution $\delta\omega_1 = \mathbf{x}^T(t)\,\mathbf{e}_4$ and $\delta\omega_2 = \mathbf{x}^T(t)\,\mathbf{e}_5$ are then inserted into Eq. (44). This allows to obtain a local expression for the nutation rate, $\dot{\theta}$, that via product-to-sum identities and manipulations, is derived as

$$\begin{aligned}\dot{\theta} \approx\ & (\breve{\varrho}_1 - \breve{\imath}_2)\cos(\omega_d t - \mu_1 t) + (\breve{\varrho}_1 + \breve{\imath}_2)\cos(\omega_d t + \mu_1 t)\\ & -(\breve{\varrho}_2 + \breve{\imath}_1)\sin(\omega_d t - \mu_1 t) + (\breve{\imath}_1 - \breve{\varrho}_2)\sin(\omega_d t + \mu_1 t)\end{aligned} \tag{49}$$

The constants $\breve{\imath}_{\,i=1,2}, \breve{\varrho}_{\,i=1,2} \in \mathbb{R}$ are given by

$$\begin{aligned}\breve{\imath}_1 &= \cos(\psi_0)\imath_1 - \sin(\psi_0)\imath_2, \quad \breve{\varrho}_1 = \cos(\psi_0)\varrho_1 - \sin(\psi_0)\varrho_2\\ \breve{\imath}_2 &= \cos(\psi_0)\imath_2 + \sin(\psi_0)\imath_1, \quad \breve{\varrho}_2 = \cos(\psi_0)\varrho_2 + \sin(\psi_0)\varrho_1\\ \imath_i &= -\mathbf{e}_{i+3}^T(\mathrm{Re}[c_1]\mathrm{Im}[\mathbf{v}_1] + \mathrm{Im}[c_1]\mathrm{Re}[\mathbf{v}_1]), \quad i = 1,2\\ \varrho_i &= \mathbf{e}_{i+3}^T(\mathrm{Re}[c_1]\mathrm{Re}[\mathbf{v}_1] - \mathrm{Im}[c_1]\mathrm{Im}[\mathbf{v}_1]), \quad i = 1,2\end{aligned} \tag{50}$$

The fact that the local solution, $\mathbf{x}(t)$, emanates from a stable equilibrium is embedded in the derivation according to Eq. (27) by selecting the gain γ as

$$\gamma = (1+\kappa)\eta\omega_d^2\Lambda^{-1}, \quad \kappa = 0.05 \tag{51}$$

which according to Eq. (27) is sufficient to ensure that $\mathrm{Re}[\lambda_1] < 0$ yet soft enough such that large control action is minimized. Computing μ_1 using Eqs. (29) and (51), the highest angular frequency component in Eq. (49) is given by the term $\omega_d + \mu_1$; it describes the high frequency oscillations. Since the angular frequency is larger than the ordinary frequency by a factor of 2π, the nutation frequency, $f_\sim$, is derived using $\omega_d + \mu_1 = 2\pi f_\sim$, as

$$\begin{aligned}f_\sim &\approx \frac{3\omega_d}{4\pi} + \frac{1}{2\pi}\sqrt{\frac{-a+\sqrt{a^2+b^2}}{2}}\\ a &= \frac{\left(\eta\dfrac{21\eta\omega_d^2}{20\Lambda} - \Lambda\right)^2}{4\eta^2} + \frac{3\omega_d^2}{4}, \quad b = \frac{\omega_d}{2}\left(\frac{21\eta\omega_d^2}{20\Lambda} + \frac{\Lambda}{\eta}\right)\end{aligned} \tag{52}$$

Precession Frequency Estimation

By repeating the above procedure, a local expression for the precession rate, $\dot{\phi}$ is obtained. Employing the spinning angle approximation (Eq. (48)) into the local solution, $\dot{\phi}$ and analyzing its angular frequency component the precession frequency, $f_\sim$, is derived and it is given by Eq. (52). This result showcases the duality of the two gyroscopic processes; it was expected from observing the structure of Eq. (44), i.e., both nutation and precession rates are trigonometric functions of the spin angle, ψ, and the angular velocity components, ω_1, ω_2.

To validate the obtained result, the developed frequency estimates are compared with the FFT data obtained from the PDAV simulations examples conducted previously. The PDAV response of system (a), via FFT on the precession/nutation responses of Fig. 1(*c*), reveals oscillations of 190.98 *Hz* (see Fig. 1(*c*) (third row)). Employing Eq. (52) together with the gain values (see Eqs. (9) and (7)) and $\omega_d = 600$ rad/s, an estimate of 191.15 *Hz* is obtained, which is 99.911% accurate to the numerically observed oscillations obtained by the FFT. Similarly, the PDAV response of system (b), via FFT on the precession/nutation responses of Fig. 1(*d*), reveals oscillations of 0.244 *Hz* (see Fig. 1(*d*) (third row)). Employing the satellite gains and $\omega_d = 0.77$ rad/s in Eq. (52), a precession/nutation frequency estimate of 0.245 Hz is obtained, which is 99.592% accurate to the numerically observed oscillations obtained by the FFT. These findings validate the developed method.

The capability to quickly estimate the precession/nutation oscillations frequency has been obtained. Having this knowledge allows one to quickly know what to expect in terms of oscillations; it aids in actuator sizing and as a guide on the feasibility of an experiment.

Flow Originating From a Neighborhood of the Closed-Loop Equilibria

The obtained eigenstructure provided insights on the CL behavior in the neighborhood of the equilibria; it is also used to initialize variational algorithms employed to chart the global flow. This process provides insights on the global behavior of the CL system; it is done next, by employing variational integration schemes (initialized via the calculated eigenstructure), to obtain (a) visualizations of the CL vector fields originating from a neighborhood of the stable manifold of the antipodal equilibrium and (b) visualizations of the CL vector fields emanating from a neighborhood of the desired equilibrium.

Because the Hartman-Grobman and the stable manifold theorems [31] are satisfied at the antipodal equilibrium, Q_2, a local stable manifold, $\mathbf{W}^s_{loc}$, exists

$$\mathbf{W}^s_{loc}(Q_2) = \{\mathbf{x} \in \mathbf{U} | \lim_{t\to\infty} \boldsymbol{\varphi}^t(\mathbf{x}) = Q_2, \forall t \geq 0\} \tag{53}$$

where $\boldsymbol{\phi}^t$ is the forward flow map and $\mathbf{U} \subset \mathrm{S}^2 \times \mathbb{R}^3$ is a neighborhood of the equilibrium, Eq. (8*c*). The local stable manifold, $\mathbf{W}^s_{\text{loc}}$, is tangent to the flat stable eigenspace, $\mathbf{E}^s$. By employing the backward flow map, $\boldsymbol{\phi}^{-t}$, on points belonging to the local stable manifold, $\mathbf{W}^s_{\text{loc}}$, the global stable manifold, $\mathbf{W}^s$ (SMSE set), can be obtained [31]. Explicitly, it is given as

$$\mathbf{W}^s(Q_2) = \underset{t\geq 0}{\cup} \boldsymbol{\phi}^{-t}(\mathbf{W}^s_{loc}(Q_2)) \tag{54}$$

The forward, $\boldsymbol{\phi}^t$, and backward flows, $\boldsymbol{\phi}^{-t}$, of the system are obtained via variational integration [21,24,32].

The analysis is performed next using the example systems presented previously, i.e., **system (a)** (see Eq. (9)) and **system (b)** (see Eq. (10)). Note that a slowly spinning/low-gain system and a fast spinning/high-gain system are purposely selected to investigate similarities in the global behavior. It is assumed that if similar behavior is observed, it can be generalized to most PDAV systems employing the controller given by Eq. (5).

Flow "Close" to the Stable Manifold of the Antipodal Equilibrium, Q_2

Next, the flow emanating from points "close" to the SMSE set is obtained. The methodology presented in Ref. [33] and later adopted in Ref. [24] is employed; the stable eigenvectors $\mathbf{v}_1$, $\mathbf{v}_4$, $\mathbf{v}_5$, are employed to produce the local stable eigenspace, $\mathbf{E}^s_{loc}$, given by

$$\begin{aligned}\mathbf{E}^s_{\text{loc}}(Q_2) = \{&(\mathbf{q}_{\text{loc}}, {}^b\boldsymbol{\omega}_{\text{loc}}) \in \mathrm{S}^2 \times \mathbb{R}^3 | \mathbf{q}_{\text{loc}}, {}^b\boldsymbol{\omega}_{\text{loc}} \\ &\varepsilon, \varsigma \ll 1, \sigma \in \mathbb{C}, \vartheta \in [0, 2\pi), \Delta_q = [\mathbf{I}, 0] \\ &\Delta_\omega = [0, \mathbf{I}] \in \mathbb{R}^{3\times 6}\} \\ &\mathbf{q}_{\text{loc}} = \exp(S(\varepsilon\cos(\vartheta)\Delta_q(\sigma\mathbf{v}_1 + \bar{\sigma}\mathbf{v}_5)))(-\mathbf{q}_d) \\ &{}^b\boldsymbol{\omega}_{\text{loc}} = \Delta_\omega(\varepsilon\cos(\vartheta)(\sigma\mathbf{v}_1 + \bar{\sigma}\mathbf{v}_5) + \varsigma\sin(\vartheta)\mathbf{v}_4) - {}^b\boldsymbol{\omega}_d\end{aligned} \tag{55}$$

To check if the methodology developed in Ref. [24] for computing the SMSE set works for the CL system in Eq. (6) also, a metric, $\mathrm{d}_{\mathbf{q},\omega}$, measuring the distance of the states from an equilibrium is defined on the tangent bundle as

$$\mathrm{d}_{\mathbf{q},\omega}((\mathbf{q}_1, {}^b\boldsymbol{\omega}_1), (\mathbf{q}_2, {}^b\boldsymbol{\omega}_2)) = \Psi(\mathbf{q}_1, \mathbf{q}_2) + \|{}^b\boldsymbol{\omega}_1 - {}^b\boldsymbol{\omega}_2\| \tag{56}$$

The forward and backward flows, i.e., $\boldsymbol{\phi}^t$ and $\boldsymbol{\phi}^{-t}$, are obtained via variational integration techniques [24,32].

Ten points from the local stable eigenspace, $\mathbf{E}^s_{\text{loc}}$ (see Eq. (55)), of each system are chosen with $\varepsilon = \varsigma = 10^{-6}$, $\sigma = 1 + 1i$. The flow evolving on the two-sphere, S^2, for each of the ten points is shown in Fig. 2. The color of the flow expresses the angular spin velocity in accordance with the colorbar. A number of attributes of the flow that passes "close" to the stable manifold as it converges to the local stable eigenspace are observed and are given next.

The flow of both examples exhibits similar behavior (the only difference is the timescale). As the flow diverges/retracts from the hyperbolic equilibria, the trajectories from logarithmic in nature begin to encircle S^2 in an elaborate fashion. Despite significantly large positive or negative initial spinning velocities, the spin velocity converges to $-\omega_d$ as the pointing state, $\mathbf{q}$, approaches the saddle (see the colorbar of Figs. 2(*b*) and 2(*d*)). In both cases, despite the fact that the SMSE set is of zero measure, the system states might approach the saddle equilibrium, Q_2, arbitrary close before eventually converging to the desired equilibrium, Q_1. These trajectories converge very slowly to the desired equilibrium.

Considerable effort was devoted to produce the SMSE set, $\mathbf{W}^s(Q_2)$, for both systems, via the method proposed in Ref. [24]; numerous simulations were performed with points very close to the antipodal equilibrium (using $\varepsilon = \varsigma \ll 10^{-6}$ in Eq. (55)) in an attempt to approach arbitrarily close to the local stable manifold,

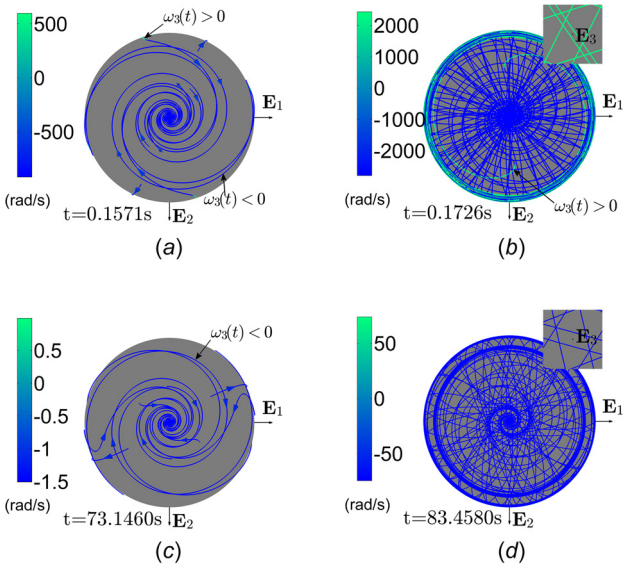

Fig. 2 Flow on S^2, backward in time, ϕ^{-t}, for the outrunner example (Figs. 2(*a*) and 2(*b*)) and for the satellite example (Figs. 2(*c*) and 2(*d*)). The spin velocity, $\omega_3(t)$ (rad/s) is indicated in accordance to the colorbar. Figure timestamps: (*a*) $t = 0.1571$ s, (*b*) $t = 0.1726$ s, (*c*) $t = 73.1460$ s, and (*d*) $t = 83.4580$ s.

$\mathbf{W}^s_{\text{loc}}$, aiming to find points, $\mathbf{p}_s$, that belong to it. To verify that the generated points are members of the local stable manifold, $\mathbf{W}^s_{\text{loc}}$, the forward flow map, $\boldsymbol{\phi}^t$, is employed on the produced points and the proximity of the flow is monitored with respect to the saddle equilibrium via Eq. (56). If the flow $\boldsymbol{\phi}^t(\mathbf{p}_s) \to Q_2$ as $t \to \infty$, then it is ensured that $\mathbf{p}_s \in \mathbf{W}^s_{\text{loc}}$ and thus those points can be used together with the backward flow map, $\boldsymbol{\phi}^{-t}$, to obtain the global stable manifold.

The flow originating from these points for system (a) can be seen in Fig. 3(*a*), and the flow proximity from the antipodal equilibrium, i.e., $\mathrm{d}_{\mathbf{q},\omega}(Q_2, \boldsymbol{\phi}^t(\mathbf{p}_s))$, is shown in Fig. 3(*b*). It is clear that even though the flow originates from points very "close" to Q_2 that are also members of $\mathbf{E}^s_{\text{loc}}$, the trajectories eventually converge to the desired equilibrium, Q_1. As a result, even though at the hyperbolic equilibrium, the local stable manifold $\mathbf{W}^s_{\text{loc}}(Q_2)$ and the local stable eigenspace $\mathbf{E}^s_{\text{loc}}(Q_2)$ are tangent, the points obtained via $\mathbf{E}^s_{\text{loc}}$ are in "close proximity" to the local stable manifold, $\mathbf{W}^s_{\text{loc}}$, but do not necessarily belong to it. Similar results hold also for system (b) but due to space constraint they are not included.

Concluding, the methodology employed in Ref. [24] to compute the SMSE set is not successful for the PDAV CL system of Eq. (6). Despite this, the proposed approach, i.e., charting the CL flow passing "close" to the stable manifold, yields sufficient information on how the SMSE set influences the CL behavior.

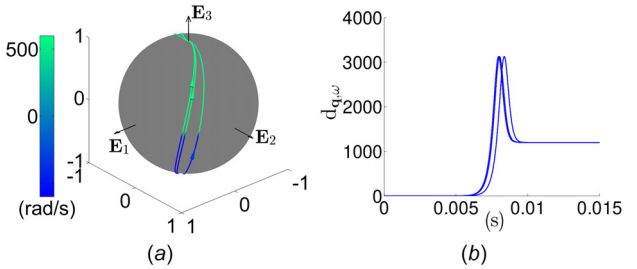

Fig. 3 Forward flow, $\{\phi^t(\mathbf{p}_s)\}_{t>0}$, for system (*a*). (*a*) Trajectories on S^2 with $\omega_3(t)$ (rad/s) identified in accordance to the colorbar. (*b*) Proximity metric, $\mathrm{d}_{\mathbf{q},\omega}(Q_2, \phi^t(\mathbf{p}_s))$.

Flow "Close" to the Desired Equilibrium, Q_1

To understand the global CL behavior, the flow converging to the desired equilibrium, Q_1, is investigated also. This task is of greater significance because the complement set of the SMSE set is open and dense and governs the behavior of the CL dynamics.

The flow converging to the desired equilibrium for both examples is visualized. Since Eq. (8*b*) is a stable focus with an almost global region of attraction, it suffices to pick points in the neighborhood of the equilibria because the flow emanating from the selected points is influenced by the dominant region of attraction. Hence, the points are picked as follows:

$$(\mathbf{q}_\xi, {}^b\boldsymbol{\omega}_{\delta\omega})|_{Q_1} = \{(\mathbf{q}, {}^b\boldsymbol{\omega}) \in \mathrm{S}^2 \times \mathbb{R}^3 | \mathbf{q}, {}^b\boldsymbol{\omega} \quad \varepsilon = 10^{-6}, \quad \varsigma = 10^{-7}, \quad \vartheta \in [0, 2\pi)\} \tag{57a}$$

$$\mathbf{q} = \exp(S(\varepsilon(\cos(\vartheta)\mathbf{b}_1 + \sin(\vartheta)\mathbf{b}_2))\mathbf{q}_d \tag{57b}$$

$${}^b\boldsymbol{\omega} = {}^b\boldsymbol{\omega}_d + \varepsilon(\cos(\vartheta)\mathbf{b}_1 + \sin(\vartheta)\mathbf{b}_2) + \varsigma\mathbf{b}_3 \tag{57c}$$

Ten points from Eq. (57) are selected for each system, and the backward flow map, $\boldsymbol{\varphi}^{-t}$, is employed to produce the trajectories that eventually end up to the selected points.

A number of attributes of the trajectories generated by the governing dense sets are observed. The computed CL flow can be seen in Fig. 4. The flow emanating from the stable equilibria of both example systems exhibits similar behavior; the only difference is the timescale. Specifically, the flow retracts from the desired equilibrium toward the antipodal equilibrium in a spiraling manner (see Figs. 4(*a*) and 4(*c*)). As the flow goes past the saddle equilibrium (see the magnified insert in Figs. 4(*b*) and 4(*d*)) and as t increases, the flow is drawn into limit cycles/circular orbits that eventually spread on the manifold obtaining significantly larger spin velocities (see colorbar in Figs. 4(*b*) and 4(*d*)). The spin velocity veers from the desired value, changes sign as the pointing state crosses the equator, stays negative as the pointing state advances past the saddle point (see Figs. 4(*b*) and 4(*d*)), and eventually increases in magnitude as the pointing states move into circular patterns or/and slowly cover the configuration space, see Figs. 4(*b*) and 4(*d*).

The nontrivial repercussions of the existence of the antipodal saddle equilibrium, its SMSE set, and its influence on the solutions of the CL system are evident. It is observed that in the neighborhood of the antipodal equilibrium, the flow takes a long time to escape the influence of the SMSE set. The fact that the flow begins to entangle in the hemisphere opposite of the desired equilibrium (see Figs. 4(*b*) and 4(*d*)) indicates that the probability that the pointing state will first pass "close" to the saddle equilibrium before reaching the desired stable equilibrium rises for pointing commands larger than 90 deg. Thus, to ensure a smooth and fast PDAV response, it is recommended to employ the PDAV controller in precision tracking scenarios and avoid step commands for which the initial tracking error is larger than 90 deg.

The CL vector field investigation was performed purposely on a slowly spinning/low-gain system and on a fast spinning/high-gain system to demonstrate that the global behavior of the flow is similar in nature; it differs only on the rate of the transient responses. The similarity of the findings implies that the CL vector field visualization results and observations are general in nature and they can be generalized to PDAV systems employing the controller given by Eq. (5).

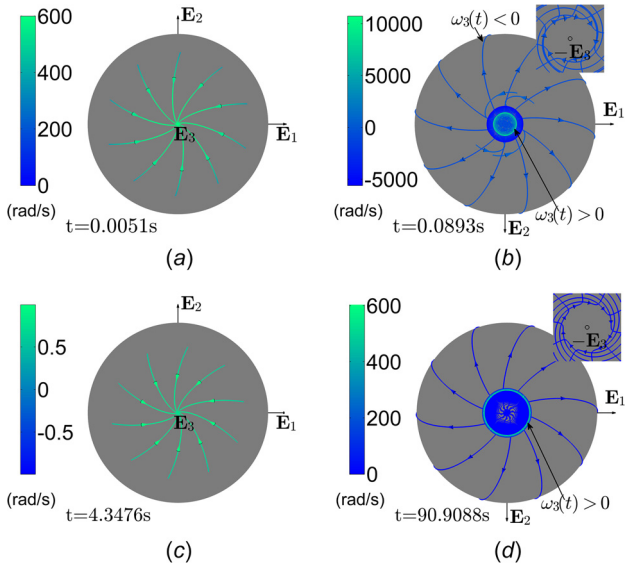

Fig. 4 Flow on S^2, backward in time, ϕ^{-t}, for the outrunner example (Figs. 4(*a*) and 4(*b*)) and for the satellite example (Figs. 4(*c*) and 4(*d*)). The spin velocity, $\omega_3(t)$ [rad/s], is indicated in accordance to the colorbar. Figure timestamps: (*a*) $t = 0.0051$ s, (*b*) $t = 0.0893$ s, (*c*) $t = 4.3476$ s, and (*d*) $t = 90.9088$ s.

Conclusion

This work analyzed the local/global CL behavior induced by a developed geometric, PDAV controller and studied the high frequency precession/nutation oscillations that characterize PDAV motions. This was done via geometrically exact linearization and via simulation techniques that amount to charting the smooth global CL vector fields. A method to quickly estimate the frequency of the nutation/precession oscillations was developed and can be used for sizing actuators. A clear understanding of the behavior of the CL flow was achieved, allowing the control engineer to anticipate/have a rough estimate of the CL response of systems in which the PDAV controller is employed. Specifically, it was concluded that a smooth PDAV response is ensured when the PDAV controller is employed in precision PDAV tracking scenarios; step commands for which the initial error is greater than 90 deg should be avoided.

Appendix

Cross product map that identifies the Lie algebra $\mathfrak{so}(3)$ with $\mathbb{R}^3$. For $\mathbf{r} \in \mathbb{R}^3$

$$S(\mathbf{r}) = [0, -r_3, r_2; r_3, 0, -r_1; -r_2, r_1, 0], \quad S^{-1}(S(\mathbf{r})) = \mathbf{r} \tag{A1}$$

For $\mathbf{R} \in \mathrm{SO}(3)$ and $\mathbf{r}, \mathbf{a}, \mathbf{b}, \mathbf{c} \in \mathbb{R}^3$, the following hold:

$$S(\mathbf{Rr}) = \mathbf{R}S(\mathbf{r})\mathbf{R}^T \tag{A2a}$$

$$(\mathbf{a}^T\mathbf{b})\mathbf{c} = (\mathbf{c}\mathbf{a}^T)\mathbf{b} \tag{A2b}$$

$$S(\mathbf{a})(S(\mathbf{b})\mathbf{c}) = (\mathbf{a}^T\mathbf{c})\mathbf{b} - (\mathbf{a}^T\mathbf{b})\mathbf{c} \tag{A2c}$$

Exponential map via the Rodrigues formulation

$$\exp(\epsilon S(\boldsymbol{\xi})) = \mathbf{I} + S(\boldsymbol{\xi})\sin\epsilon + S(\boldsymbol{\xi})^2(1 - \cos\epsilon) \tag{A3}$$

Derivative of Eqs. (5*d*) and (4*b*) with respect to time

$$\dot{\Psi} = \mathbf{R}^b\mathbf{e}_q \cdot \mathbf{R}^b\mathbf{e}_\omega \tag{A4a}$$

$${}^b\dot{\mathbf{e}}_q = \mathbf{R}^T(S(\dot{\mathbf{q}}_d)\mathbf{q} + S(\mathbf{q}_d)\dot{\mathbf{q}}) - S({}^b\boldsymbol{\omega})^b\mathbf{e}_q \tag{A4b}$$

For $a, b \in \mathbb{R}$, the following identity holds [34]:

$$a + bi = \left(\sqrt{\frac{a + \sqrt{a^2 + b^2}}{2}} + i\sqrt{\frac{-a + \sqrt{a^2 + b^2}}{2}}\right)^2 \tag{A5}$$

References

[1] Osborne, J., Hicks, G., and Fuentes, R., 2008, "Global Analysis of the Double-Gimbal Mechanism," IEEE Control Syst. Mag., **28**(4), pp. 44–64.

[2] Repoulias, F., and Papadopoulos, E., 2007, "Planar Trajectory Planning and Tracking Control Design for Underactuated Auvs," Ocean Eng., **34**(11–12), pp. 1650–1667.

[3] Ramp, M., and Papadopoulos, E., 2015, "On Modeling and Control of a Holonomic Vectoring Tricopter," International Conference on Intelligent Robots and Systems (IROS), Hamburg, Germany, Sept. 28–Oct. 2, pp. 662–668.

[4] Chi, B., Hu, Q., and Guo, L., 2018, "Reduced Attitude Control in the Presence of Pointing Constraint," 37th Chinese Control Conference (CCC), Wuhan, China, July 25–27, pp. 9781–9785.

[5] Invernizzi, D., and Lovera, M., 2019, "Attitude Stabilization of Inertial Pointing Spacecraft Using Magnetic Actuators," IFAC-PapersOnLine, **52**(12), pp. 442 –447.

[6] Dhullipalla, M. H., Hamrah, R., Warier, R. R., and Sanyal, A. K., 2019, "Trajectory Generation on se(3) for an Underactuated Vehicle With Pointing Direction Constraints," American Control Conference (ACC), Philadelphia, PA, July 10–12, pp. 1930–1935.

[7] Chaturvedi, N. A., Sanyal, A. K., and McClamroch, N. H., 2011, "Rigid-Body Attitude Control," IEEE Control Syst. Mag., **31**(3), pp. 30–51.

[8] Chaturvedi, N. A., McClamroch, N. H., and Bernstein, D. S., 2009, "Asymptotic Smooth Stabilization of the Inverted 3-d Pendulum," IEEE Trans. Autom. Control, **54**(6), pp. 1204–1215.

[9] Chaturvedi, N., McClamroch, N., and Bernstein, D., 2008, "Stabilization of a 3d Axially Symmetric Pendulum," Automatica, **44**(9), pp. 2258–2265.

[10] Mayhew, C. G., and Teel, A. R., 2010, "Global Asymptotic Stabilization of the Inverted Equilibrium Manifold of the 3-d Pendulum by Hybrid Feedback," 49th Conf. Decis. Control (CDC), Atlanta, GA, Dec. 15–17, pp. 679–684.

[11] Mayhew, C. G., and Teel, A. R., 2013, "Global Stabilization of Spherical Orientation by Synergistic Hybrid Feedback With Application to Reduced-Attitude Tracking for Rigid Bodies," Automatica, **49**(7), pp. 1945–1957.

[12] Ramp, M., and Papadopoulos, E., 2015, "Attitude and Angular Velocity Tracking for a Rigid Body Using Geometric Methods on the Two-Sphere," European Control Conference (ECC), Linz, Austria, July 15–17, pp. 3238–3243.

[13] Bhat, S., and Bernstein, D. S., 2000, "A Topological Obstruction to Continuous Global Stabilization of Rotational Motion and the Unwinding Phenomenon," Syst. Control Lett., **39**(1), pp. 63–70.

[14] Bernuau, E., Perruquetti, W., and Moulay, E., 2013, "Retraction Obstruction to Time-Varying Stabilization," Automatica, **49**(6), pp. 1941–1943.

[15] Mayhew, C. G., Sanfelice, R. G., and Teel, A. R., 2011, "Quaternion-Based Hybrid Control for Robust Global Attitude Tracking," IEEE Trans. Autom. Control, **56**(11), pp. 2555–2566.

[16] Lee, T., 2015, "Global Exponential Attitude Tracking Controls on so(3)," IEEE Trans. Autom. Control, **60**(10), pp. 2837–2842.

[17] Lee, T., Chang, D. E., and Eun, Y., 2019, "Semiglobal Nonmemoryless Attitude Controls on the Special Orthogonal Group," ASME J. Dyn. Syst., Meas., Control, **141**(2), p. 021005.

[18] Koditschek, D. E., 1988, "Application of a New Lyapunov Function to Global Adaptive Attitude Tracking," Proceedings of the 27th Conference on Decision and Control (CDC), Vol. 1, Austin, TX, Dec. 7–9, pp. 63–68.

[19] Lee, T., Leok, M., and McClamroch, N. H., 2010, "Geometric Tracking Control of a Quadrotor UAV on SE(3)," 49th Conference on Decision and Control (CDC), Atlanta, GA, Dec. 15–17, pp. 5420–5425.

[20] Warier, R. R., Sanyal, A. K., Dhullipalla, M. H., and Viswanathan, S. P., 2018, "Finite-Time Stable Trajectory Tracking and Pointing Control for a Class of Underactuated Vehicles in SE(3)," Indian Control Conference (ICC), Kanpur, India, Jan. 4–6, pp. 190–195.

[21] Sanyal, A., Nordkvist, N., and Chyba, M., 2011, "An Almost Global Tracking Control Scheme for Maneuverable Autonomous Vehicles and Its Discretization," IEEE Trans. Autom. Control, **56**(2), pp. 457–462.

[22] Goodarzi, F. A., and Lee, T., 2016, "Stabilization of a Rigid Body Payload With Multiple Cooperative Quadrotors," ASME J. Dyn. Syst., Meas., Control, **138**(12), p. 121001.

[23] Ramp, M., and Papadopoulos, E., 2018, "Global Closed-Loop Equilibrium Properties of a Geometric PDAV Controller Via a Coordinate-Free Linearization," European Control Conference (ECC), Limassol, Cyprus, June 12–15, pp. 1250–1256.

[24] Lee, T., Leok, M., and McClamroch, N. H., 2011, "Stable Manifolds of Saddle Equilibria for Pendulum Dynamics on S^2 and SO(3)," 50th Conference on Decision and Control (CDC) and European Control Conference (EUCA), Orlando, FL, Dec. 12–15, pp. 3915–3921.

[25] Goldstein, H., Poole, C., and Safko, J., 2013, *Classical Mechanics*, Pearson, London.

[26] Lewis, A. D., and R. T, D., 2010, "Geometric Jacobian Linearization and LQR Theory," J. Geomet. Mech., **2**(4), pp. 397–440.

[27] Wu, G., and Sreenath, K., 2015, "Variation-Based Linearization of Nonlinear Systems Evolving on SO(3) and S^2," IEEE Access, **3**, pp. 1592–1604.

[28] Cooke, R., and Arnold, V., 1992, *Ordinary Differential Equations*, Springer Textbook. Springer, Berlin/Heidelberg.

[29] Ilchmann, A., and Mueller, M., 2007, "Time-Varying Linear Systems: Relative Degree and Normal Form," IEEE Trans. Autom. Control, **52**(5), pp. 840–851.

[30] Brunovskỳ, P., 1970, "A Classification of Linear Controllable Systems," Kybernetika, **6**(3), pp. 173–188.

[31] Guckenheimer, J., and Holmes, P., 2002, *Nonlinear Oscillations, Dynamical Systems, and Bifurcations of Vector Fields* (Applied Mathematical Sciences), Springer, New York.

[32] Lee, T., Leok, M., and McClamroch, N. H., 2007, "Lie Group Variational Integrators for the Full Body Problem in Orbital Mechanics," Celestial Mech. Dyn. Astron., **98**(2), pp. 121–144.

[33] Krauskopf, B., Osinga, H. M., Doedel, E. J., Henderson, M. E., Guckenheimer, J., Vladimirsky, A., Dellnitz, M., and Junge, O., 2005, "A Survey of Methods for Computing (Un)Stable Manifolds of Vector Fields," Int. J. Bifurcation Chaos, **15**(03), pp. 763–791.

[34] Penrose, R., 2004, *Road to Reality*, 1st ed., Jonathan Cape (Rand), London.